PCCP

ROYAL SOCIETY OF CHEMISTRY

PAPER

View Article Online
View Journal | View Issue

Cite this: *Phys. Chem. Chem. Phys.*, 2025, **27**, 17303

Received 20th April 2025,
Accepted 26th July 2025

DOI: 10.1039/d5cp01512j

rsc.li/pccp

# Exploring radical formation and ultrafast intersystem crossing in a heavy-atom-free thiophene derivative

Luca M. Sihn, *[a] Robert B. Vadell,[b] Rafael B. Araujo,[c] Atripan Mukherjee,[de] Miroslav Kloz,[e] Jacinto Sá[bf] and Henrique E. Toma[a]

The photophysical study of decarboxyranelic acid (DRAc), a thiophene derivative made from strontium ranelate, shows that it can form long-lived radical cation species through a pathway involving triplet states. Femtosecond transient absorption spectroscopy and computational modeling reveal a fast intersystem crossing (ISC) process in water, with a time constant of 1.1 ps and a quantum yield of 27%. The small energy gap between the $S_1$ and $T_1$ states, along with the mixed πσ* character of the $S_1$ state, contributes to this rapid ISC, in line with El-Sayed's rule. The results indicate that DRAc's photoreactivity is strongly influenced by the solvent: in water, the high hydrogen-bond donor capacity stabilizes the $S_1$ state, narrows the energy gap, and creates an almost barrier-free ISC pathway. Studies using deuterated solvents show that the ISC rate increases due to stronger stabilization of the $S_1$ state by deuterium bonds. Overall, these results make DRAc a useful model for studying heavy-atom-free molecules with efficient ISC and radical formation, with potential applications in photodynamic therapy and catalysis.

## Introduction

The nonreactive transition known as intersystem crossing (ISC) – between electronic states of different multiplicities – plays a pivotal role across multiple fields, including photonic,[1] materials science,[2] photodynamic therapy for cancer,[3] and catalysis.[4] However, this spin-forbidden process is naturally slow, often reaching the microsecond range in $S_1 \rightarrow T_1$ transitions[5] due to spin selection rules. Enhancing the efficiency of ISC is possible by increasing spin–orbit coupling (SOC), typically achieved by incorporating heavy atoms like ruthenium, iridium, iodine, or bromine into molecular structures. These heavy atoms drive up ISC efficiency by leveraging the heavy-atom effect.[6]

In recent years, however, the high cost,[7–10] toxicity,[11] high environmental impact[12–14] and stability[15] concerns surrounding heavy-atom compounds have spurred interest in heavy-atom-free molecules (HAFMs). HAFMs offer a promising alternative, achieving rapid ISC (often reaching sub-picosecond timescales)[16] without the negative impact of heavy metals. This capability is driven by specific molecular features that promote SOC without relying on heavy atoms.

One effective molecular feature is a small energy gap between the $S_1$ and $T_1$ or $T_2$ states, which enhances vibrational wavefunction overlap, thus facilitating ISC.[17–19] This concept, known as the energy gap law, is exemplified in benzophenone – a well-researched molecule with ultrafast dynamics and efficient ISC in catalysis applications.[20] Benzophenone achieves sub-picosecond ISC through two main factors: a nearly degenerate $S_1$ (nπ*) and $T_2$ (ππ*) state, and an orbital configuration that follows El-Sayed's rule.[21] This rule posits that transitions between states with different orbital configurations (nπ* for $S_1$ and ππ* for $T_2$) exhibit increased SOC,[22] leading to efficient ISC.

Beyond catalysis, HAFMs are gaining traction in PDT to generate reactive oxygen species (ROS) without the health and environmental hazards of heavy-atom compounds.[16] In PDT, ultrafast ISC enables efficient energy transfer to molecular oxygen, producing singlet oxygen ($^1O_2$), a potent ROS essential for therapeutic applications.

Our study leverages this emerging field by exploring decarboxyranelic acid (DRAc) (Fig. 1), a non-toxic[23] thiophene derivative synthesized from Strontium Ranelate, a medication widely used to treat osteoporosis in postmenopausal women.[24–29] DRAc's

---

[a] *Institute of Chemistry, University of São Paulo, 05508-000 São Paulo, Brazil. E-mail: luca.sihn@usp.br*

[b] *Department of Chemistry-Ångström, Physical Chemistry division, Uppsala University, Box 532, 751 20 Uppsala, Sweden*

[c] *Department of Materials Science and Engineering, Solid State Physics, Uppsala University, 75103 Uppsala, Sweden*

[d] *Department of Chemistry and Biochemistry, Mendel University in Brno, Zemedelska 1, CZ-613 00 Brno, Czech Republic*

[e] *ELI Beamlines Facility, The Extreme Light Infrastructure ERIC, Za Radnici 835, 252 41 Dolni Brezany, Czech Republic*

[f] *Institute of Physical Chemistry, Polish Academy of Sciences, ul. Kasprzaka 44/52, 01-224 Warsaw, Poland*

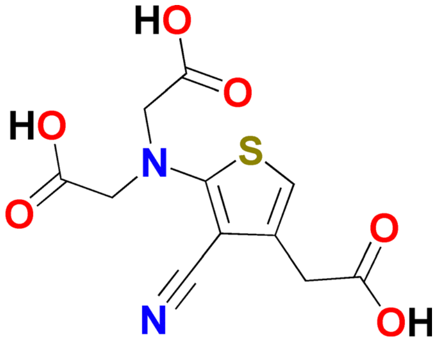

Fig. 1 Molecular structure of DRAc.

synthesis is straightforward,[30] and initial investigations revealed a surprisingly rapid ISC process,[31] presenting exciting implications for PDT and catalysis. Structurally, DRAc contains a thiophene core with carboxylic and amino-carboxylic arms resembling EDTA, along with a nitrile group. This molecule undergoes photodimerization at the C2 carbon, suggesting a reactive excited state suitable for various applications. Using ultrafast spectroscopy and computational calculations, we identified a sub-picosecond ISC time constant and mapped out a feasible ISC pathway, along with a long-lived radical cation species. These findings reveal new opportunities to develop HAFMs as efficient, environmentally responsible alternatives in PDT and catalysis, further advancing the utility and commercial potential of ISC-based applications without the drawbacks of heavy metals.

## Results and discussion

The steady-state absorption spectrum of DRAc, along with the calculated vertical excitation energy, is presented in Fig. 2a. Two prominent absorption peaks are observed at 223 nm and 297 nm, with the latter attributed to the $S_1$ transition. Our computational analysis further reveals two low-energy triplet excited states, $T_2$ and $T_1$, located at 313 nm and 416 nm, respectively. In Fig. 2b, natural transition orbitals (NTO) analysis shows that both triplet states exhibit $\pi\pi^*$ character, aligning with the electronic configuration of the $S_1$ state. Notably, the $S_1$ transition also displays a $\pi\sigma^*$ [32,33] contribution, distinguishing it from the purely $\pi\pi^*$ nature of the triplet states. This mixed character in $S_1$ likely plays a significant role in enhancing the molecule's intersystem crossing efficiency, a hypothesis that will be further examined through ultrafast measurements.

Furthermore, it is important to emphasize that the orbitals involved in the $S_1$ transition are delocalized across the thiophene ring and extend into the directly attached functional groups. This characteristic is further corroborated by near-resonant Raman spectroscopy (NRRS), as illustrated in the Raman spectrum (Fig. 3). Here, the selective enhancement of vibrational modes associated with electronic excitation confirms this orbital distribution, providing additional insight into the electronic structure.[34–36]

In the NRRS spectrum, four key signals are observed: the $CH_2$ stretching $\nu_{CH_2}$ (2980 cm$^{-1}$) and bending $\delta_{CH_2}$ (1404 cm$^{-1}$) modes, which show moderate intensity amplification, and the more prominent nitrile signal (2209 cm$^{-1}$) along with the $\nu_{\mathrm{C{=}C}} + \nu_{\mathrm{C\text{–}N}}$ mode (1516 cm$^{-1}$), which exhibit the highest amplification. This selective enhancement aligns with the involvement of these groups in the electronic transition. As anticipated, the thiophene ring and nitrile group play a significant role in the transition, while the $CH_2$ group displays comparatively lower participation.

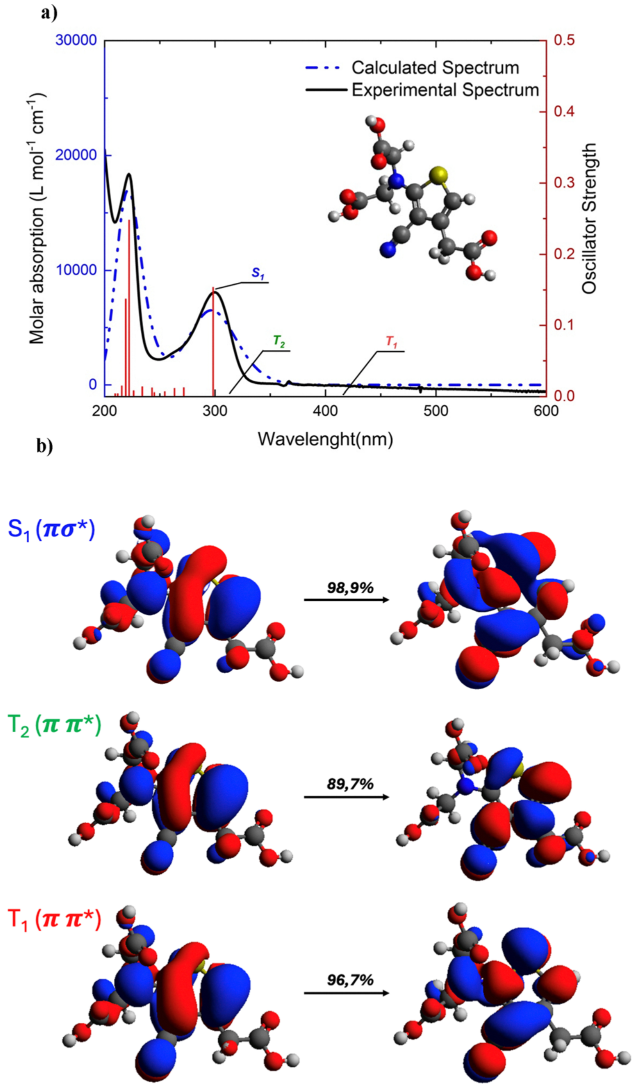

Fig. 2 (a) Absorbance spectrum of H5 in aqueous solution with HCl 6 mol L$^{-1}$ (black) and the calculated spectra for the displayed structure (blue) with the calculated transitions (red). (b) Hole-particle pairs of NTOs (isosurface value = 0.02 a.u.) of $S_1$, $T_1$ and $T_2$.

Before exploring the photodynamic of DRAc with ultrafast techniques, a computational model of the molecule and its excited states is needed. To construct this model, vertical excitation energies were calculated at the $S_{1\mathrm{min}}$, $T_{2\mathrm{min}}$, and $T_{1\mathrm{min}}$ geometries. The resulting energy diagram is displayed in Fig. 4, with detailed computational results provided in SI. In the figure, a potential energy diagram (PED) shows the behaviour of all excited states involved in these dynamics across all main geometries.

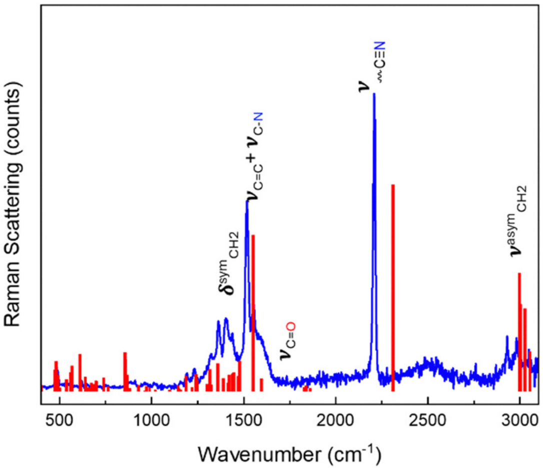

Fig. 3 Near-resonant Raman spectrum of powdered DRAc (blue) and the calculated spectra of DRAc (red).

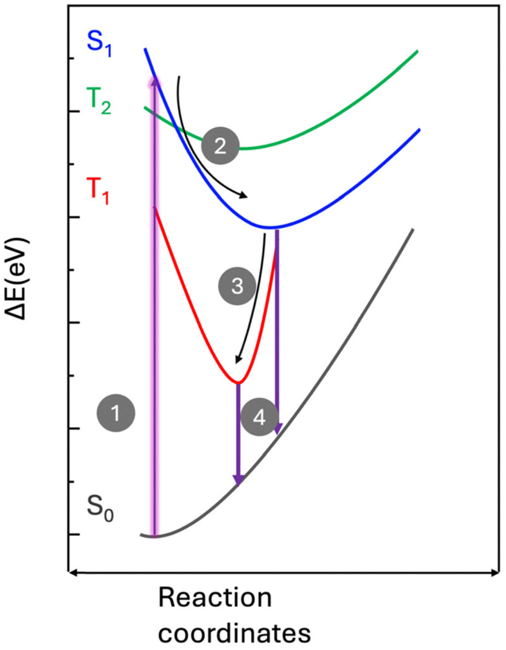

Fig. 4 Schematic illustration of the potential energy for this system, with calculated relative energies of $S_1(\sigma\pi^*)$, $T_1(\pi\pi^*)$ and $T_2(\pi\pi^*)$.

This PED reveals that after a vertical excitation from $S_0$ (1), the molecule transitions to an energetically "hot" $S_1$ state. Upon reaching this state, the molecule undergoes energy loss (2), relaxing to the $S_{1min}$ geometry, followed by solvent reorganization around this new geometry.

This process of structural relaxation, typical in thiophene derivatives, has a time constant of approximately 80 fs.[33,37] This process cannot be detected due to the equipment's resolution. Upon reaching $S_{1min}$ configuration, calculations suggest a small energy gap between the $S_1$ and $T_1$ states (0.06 eV), indicating a potential pathway for intersystem crossing (ISC) (3). Thiophene derivatives are known to undergo efficient ISC.[38–40] For instance, Grebner *et al.*[41] investigated this process in oligothiophenes, finding time constants ranging from 51 ps in bithiophene to 1100 ps in sexithiophene. Similarly, Zheldakov *et al.*[42] examined the excited-state dynamics and triplet formation in phenylthiophenes, reporting ISC time constants between 21 ps and 132 ps, which fall within the detection capabilities of our equipment. There is also the possibility that this ISC occurs between the $S_1$ and $T_2$ states. However, this is highly unprobeable, as the rate of structural relaxation significantly exceeds the rate of ISC. The decay from both excited states $S_1$ and $T_1$ to the ground state $S_0$ (4) is possible as well and will be consider in the kinetic model.

Building on this understanding of excited-state dynamics, we further investigated the solvent influence on these excited states. Vertical excitation energies were calculated with $H_2O$ and $CH_3OH$ as solvents. These calculations employed the polarizable continuum model (PCM) with the integral equation formalism (IEFPCM) for indirect solvation, followed by a hybrid solvation approach that combines IEFPCM with explicit water molecules surrounding the DRAc molecule. This dual approach enables differentiation between dielectric effects and those arising from hydrogen bonding. The energy diagram for water is displayed in Fig. 5, with detailed computational results supporting these findings provided in the SI.

There is minimal difference between the energy levels in vacuum and in $H_2O_{imp}$ ($H_2O$ as indirect solvent), indicating that the primary influence of the solvent is not solely due to its dielectric properties. However, when comparing the energy levels in $H_2O_{imp}$ with those in $H_2O_{exp}$ ($H_2O$ as implicit and explicit solvent), a notable increase in difference is observed,

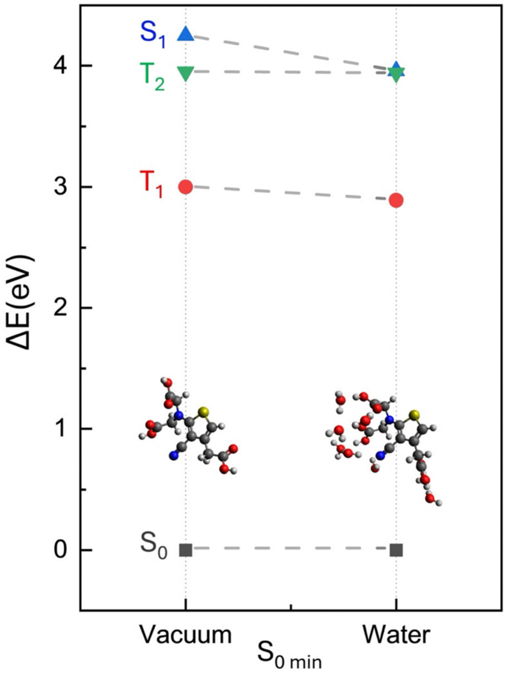

Fig. 5 Comparison between vertical excitation energy levels of $S_1(\sigma\pi^*)$, $T_1(\pi\pi^*)$ and $T_2(\pi\pi^*)$ and $S_0$ with water as an implicit solvent model (vacuum) and as a hybrid solvent model (water).

suggesting that hydrogen bonding in the $(H_2O)_8$–DRAc system plays a significant role in energy level stabilization. While all states are affected by hydrogen bonding, the $S_1$ state shows the largest stabilization, with a $\Delta E$ of 0.3 eV, followed by the $T_1$ state with a $\Delta E$ of 0.14 eV.

A similar analysis conducted with methanol shows a less pronounced difference (Table S5), underscoring the importance of hydrogen bonding as a solvent parameter in these interactions. This trend aligns with the higher hydrogen bond donor capacity (Kamlet–Taft parameter $\alpha$) of $H_2O$ compared to $CH_3OH$ ($\alpha_{H_2O}$ =1.09 and $\alpha_{CH_3OH}$ = 0.93).[43]

To evaluate the importance of the solvent in the processes presented earlier, the influence of hydrogen bonding on the $S_1$ energy level was considered in the PED (Fig. 6). As the solvent's hydrogen donor capacity ($\alpha$) increases, the $S_1$ state becomes further stabilized. In solvents with low hydrogen donor capacity ($\alpha$), calculations indicate that the STC (singlet–triplet crossing) between $S_1$ and $T_1$ does not occur at $S_{1\text{min}}$, as shown previously, suggesting the crossing occurs away from this geometry. As $\alpha$ increases, the energy gap between the $S_1$ and $T_1$ states narrows, bringing the STC closer to $S_{1\text{min}}$. In $H_2O_{\text{exp}}$, the STC appears very close to the $S_1$ minimum, creating an almost barrier-free ISC pathway. Thus, as the energy gap narrows, the likelihood of intersystem crossing is enhanced,[44] resulting in a fast and effective crossing.

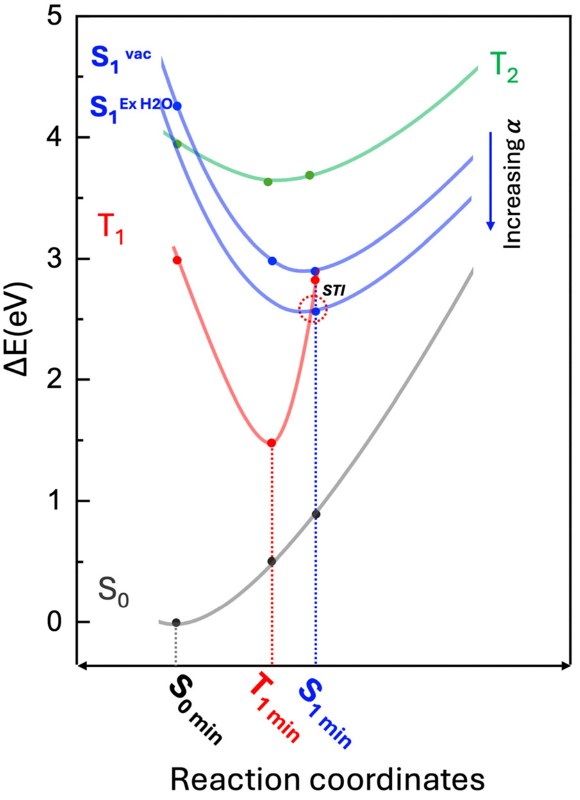

Fig. 6 Schematic illustration of the potential energy for this system, with calculated relative energies of $S_1(\sigma\pi^*)$, $T_1(\pi\pi^*)$ and $T_2(\pi\pi^*)$. Two PE curves of the $S_1(\sigma\pi^*)$ state are shown to represent those in a solvent with a medium $\alpha$ and high-$\alpha$ solvent. STI: singlet–triplet intersection.

To corroborate this model, femtosecond transient absorption spectroscopy (TAS) measurements of this system were conducted in acidic solution of $H_2O$, MeOH, as well as its deuterated counterparts, $D_2O$ and $CD_3OD$, to determine the influence of hydrogen bounding.[21] All spectra were acquired with UV excitation ($\lambda_{\text{pump}}$ = 310 nm), and the transient absorption spectra were recorded across the probe range ($\lambda_{\text{probe}}$ = 330–700nm) with delays up to $\Delta t$ = 8 ns, as shown in Fig. 8a. A key feature in the fs-TA spectrum is the broad positive band in the UV region, corresponding to an excited state absorption (ESA) (Fig. 8a). In Fig. 8c, the ESA band exhibits contributions from multiple species, as indicated by its spectral profile. Notably, during the decay of this band (Fig. 8d), the red edge diminishes more rapidly than the region around 350 nm, providing clear evidence of multiple states contributing to the decay process. These observations are consistent with our predictions.

To align the data with our model, a three-state kinetic system was proposed, as illustrated in Fig. 7. This model incorporates three kinetic constants: $k_1$, representing $S_1 \rightarrow S_0$ internal conversion (IC); $k_2$, corresponding to $S_1 \rightarrow T_1$ ISC; and $k_3$, describing $T_1 \rightarrow S_0$ ISC.

Global analysis of these dynamics reveals that indeed this system can be described as a three-state system and its dynamic is also solvent-dependent, as predicted by calculations. The extracted rate constants are summarized in Table 1 and the temporal evolution of the $S_1$ and $T_1$ state throughout the time was constructed and is shown in Fig. 8b. The population of $S_1$ rapidly decays to near zero within the first picosecond, while the population of $T_1$ is populated by the $S_1$ state, reaching a maximum around 1.5 ps and retains a detectable population during the studied delays. This dynamic agrees with the proposed model, not only the feeding relation between $S_1$ and $T_1$, but the effectiveness and the ultrafast timescale of the ISC due to an almost barrier free pathway. In $H_2O$, this ultrafast ISC has a timescale of 1.1 ps, reaching a 27% efficiency.

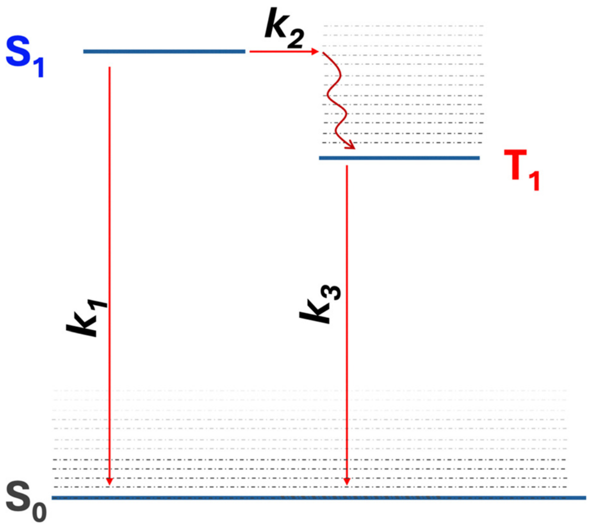

Fig. 7 Simplified energy level of DRAc with all considered kinetic constants in the kinetic model.

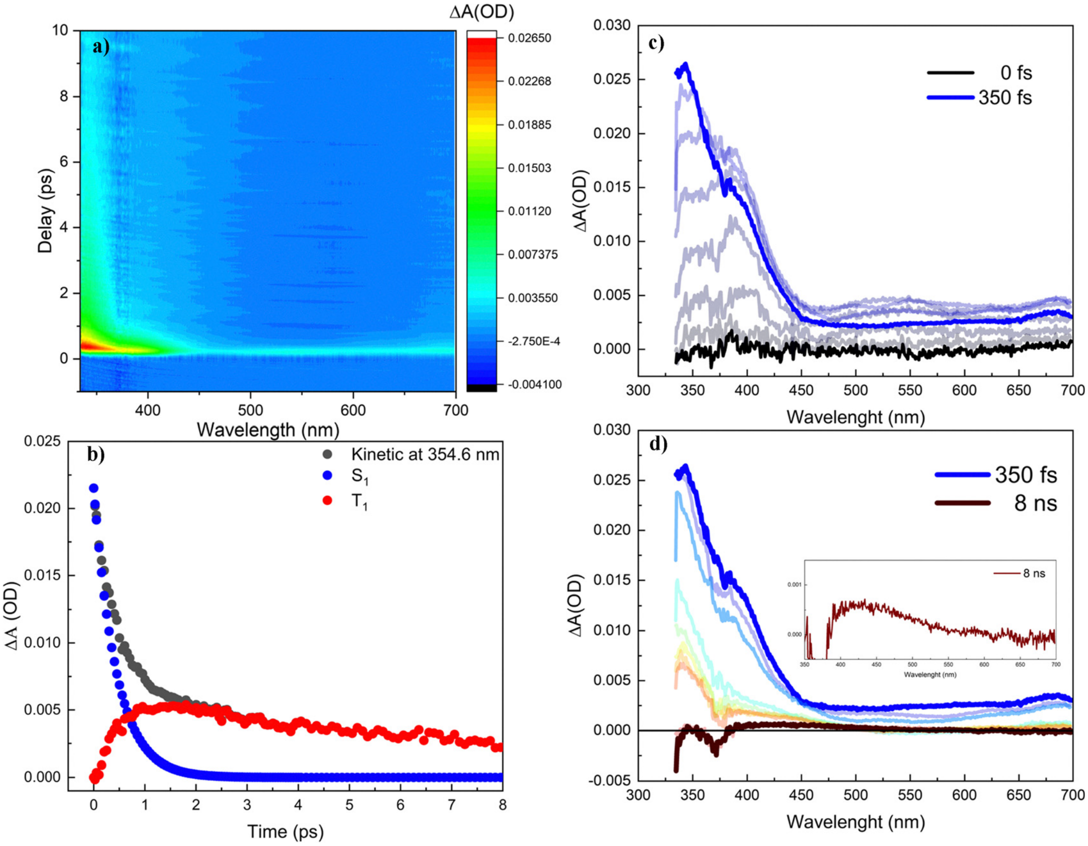

Fig. 8 (a) Contour plots of fs-TAS spectra of DRAc in methanol (HCl 3 mol $L^{-1}$). (b) Temporal evolution of the $S_1$ and $T_1$ DRAc state throughout the time in methanol (HCl 3 mol $L^{-1}$). (c) and (d) Wavelength traces sliced at representative delay times of the fs-TAS spectra in methanol (HCl 3 mol $L^{-1}$).

Table 1 Time constants of DRAc in different solvent

| Solvent | $k_1$ (ps$^{-1}$) | $k_2$ (ps$^{-1}$) | $k_3$ (ps$^{-1}$) | $\Phi_{ISC}$ |
|---|---|---|---|---|
| $H_2O$ | 2.5 ± 0.2 | 0.91 ± 0.03 | 0.74 ± 0.05 | 0.27 ± 0.02 |
| MeOH | 2.39 ± 0.07 | 0.66 ± 0.02 | 0.42 ± 0.01 | 0.22 ± 0.007 |
| $D_2O$ | 2.29 ± 0.1 | 1.1 ± 0.02 | 0.56 ± 0.02 | 0.33 ± 0.01 |
| $CD_3OD$ | 2.6 ± 0.1 | 0.81 ± 0.02 | 0.39 ± 0.02 | 0.24 ± 0.01 |

Another factor other than the favourable ISC pathway that may contribute to this ultrafast ISC rate is the mixed $\pi\sigma^*$ character of the $S_1$ state, as mentioned previously. This $\pi\sigma^*$ character may increase ISC probability between the $S_1(\pi\sigma^*)$ and $T_1(\pi\pi^*)$ states,[45] as stated by the El-Sayed's rule, further accelerating the transition. However, additional studies are necessary to quantify the impact of this factor on the dynamics.

Moreover, the solvent has a significant influence on the dynamics. As the hydrogen bond donor capacity increases (comparing $H_2O$ and MeOH), the $k_2$ is reduced by 28%. Not only does the absolute rate value change, but the ISC efficiency also varies accordingly. Specifically, there is a 23% increase in efficiency when moving from methanol to water and reaching an efficiency of 33% in $D_2O$ and a sub-picosecond ISC time constant of 0.9 ps. This isotopic effect can be explained. In both cases the $k_2$ is greater in the deuterated solvents due to the stronger deuterium bond compared to the hydrogen bond.[46]

$k_1$ analysis also cast a light at the influence of the HB in the $S_1$ energy. As the solvent hydrogen bond donor capacity increases, the $S_1 \rightarrow S_0$ rate increases, aligning with the predictions of our model. As the $S_1$ state gets stabilized by the HB's, the energy gap between the excited state and the ground state shrinks, increasing the transition rate according to the energy gap law.[47]

When compared to the deuterated solvent, there are two competing effects that should be considered. The first one is the stabilization of the $S_1$ state due to the HB, which increases the transition rate, as discussed before. The second effect is the different probability of vibronic coupling between the electronically excited molecule and vibrational modes of the solvent.[48] In the deuterated solvent, the rate of non-radiative deactivation is lower compared to the non-deuterated solvent because the amplitude and frequency of vibrational modes are reduced due to deuterium's greater mass, diminishing vibrational coupling and the effectiveness of non-radiative decay pathways.[49]

In deuterated water, the second effect exerts a more pronounced influence on $k_1$, resulting in a reduced rate of non-radiative deactivation. On the other hand, in deuterated methanol compared to methanol, the first effect predominates.

The same effect is observed in the ISC from $T_1 \rightarrow S_0$. However, the influence of hydrogen bonding is less pronounced in the $T_1$ energy level compared to $S_1$, as illustrated in Fig. 5. Consequently, the second effect consistently dominates, resulting in a lower $k_3$ value for the deuterated solvent compared to its hydrogenated counterpart. A diagram comparing the solvents is shown in Fig. 9, summarizing this analysis.

As the triplet state $T_1$ reaches a stable population, a notable reactive pathway emerges: the formation of a long-lived radical cation species. In the Fig. 10 the long live species spectrum is shown, along with the calculated transitions of DRAc radical. This radical plays a central role in driving the previously discussed dimerization reaction, highlighting the reactivity of the $T_1$ state, providing valuable insight into its potential for driving chemical transformations. This assignment is further supported by the well-established reactivity of thiophene derivatives,[50,51] where radical-mediated mechanisms are frequently implicated in both polymerization and dimerization processes. Nevertheless, it is important to emphasize that this interpretation, while supported by several lines of evidence, does not exclude the possibility of parallel pathways, including photodegradation processes.

The generation of this radical underscores the suitability of DRAc for applications where triplet-state reactivity is a key factor, such as photodynamic therapy (PDT) and catalysis.

To corroborate this model, a femtosecond Raman spectroscopy study was performed in this system, as shown in Fig. 11. At 0 ps, the main peak observed at 1050 cm$^{-1}$ primarily arises

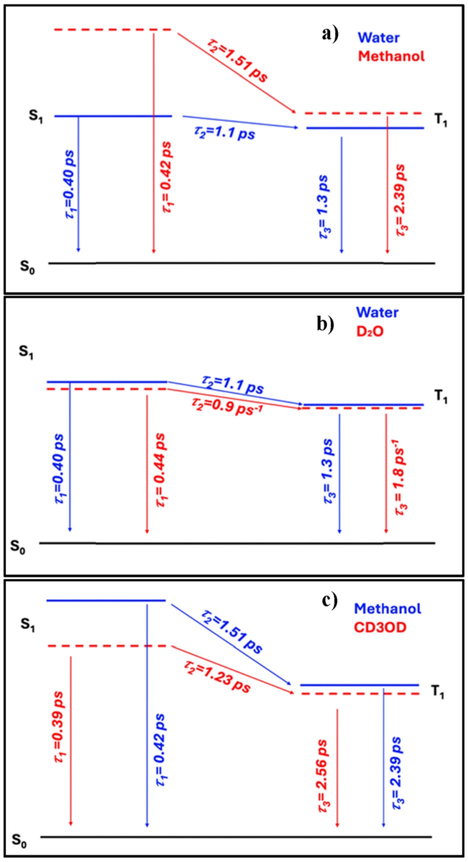

Fig. 9 Compared energy levels of DRAc and the corresponding time constants for each transition in: (a) water and methanol, (b) water and $D_2O$, and (c) methanol and $CD_3OD$.

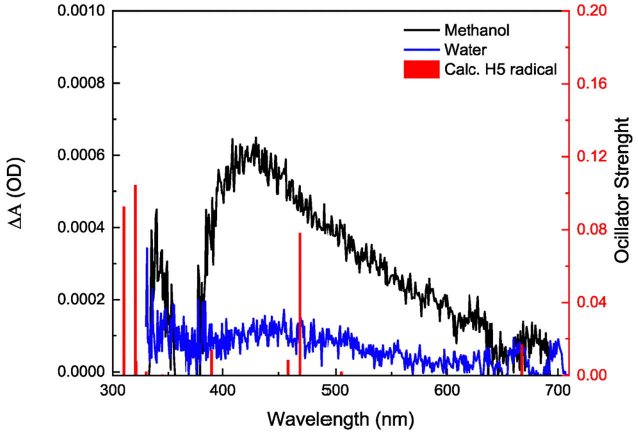

Fig. 10 Spectrum of the long-lived of the TAS experiment in methanol (black), water (blue) and the calculated electronic transitions for $[DRAc]^+$.

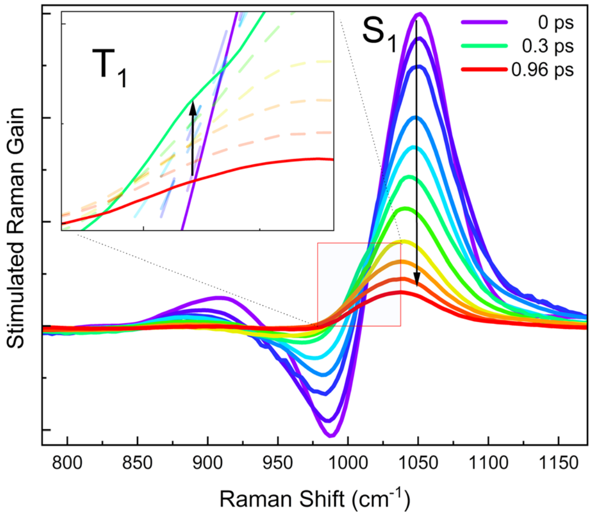

Fig. 11 Femtosecond Raman spectrum of H5 in methanol with HCl 6 mol L$^{-1}$ ($\lambda_{pump}$ = 280 nm and $\lambda_{Raman}$ = 800 nm) in the 1000 cm$^{-1}$ region.

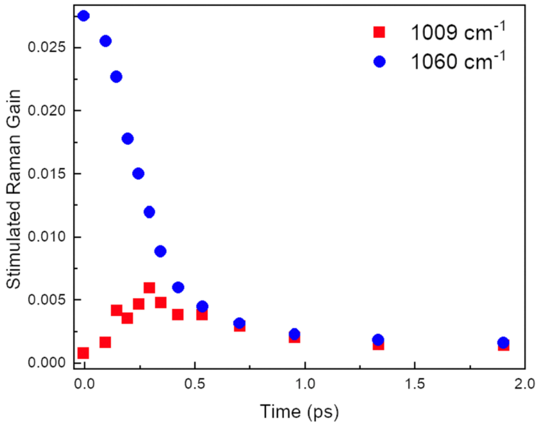

Fig. 12 Time traces (transients) sliced at 1009 cm$^{-1}$ and 1060 cm$^{-1}$ of the FSRS spectra in methanol with HCl 6 mol L$^{-1}$ ($\lambda_{pump}$ = 280 nm and $\lambda_{Raman}$ = 800 nm).

from the stimulated Raman signal of the $S_1$ state. However, this signal also shows a subtle contribution from the $T_1$ state Raman signal, which becomes evident in the initial part of its kinetic profile, as shown in Fig. 12, displaying a slight prolongation attributed to the feeding of $T_1$ from $S_1$. After 0.3 ps, a new peak emerges around 1009 cm$^{-1}$, which is assigned to the $T_1$ state. Importantly, the 1009 cm$^{-1}$ band rises in synchrony with the decay of the 1050 cm$^{-1}$ band, indicating that ISC from $S_1$ populates $T_1$ and supporting our kinetic model—where the decline of one band coincides with the rise of the other.

These findings reinforce the proposed model, providing vibrational evidence of the ISC dynamics and the involvement of the T1 state. This analysis supports the mechanistic insights proposed earlier and demonstrates the proposed dynamic.

## Conclusions

The ultrafast excited-state dynamics of decarboxyranelic acid (DRAc) were elucidated through a combination of femtosecond transient absorption spectroscopy and computational analysis. Upon photoexcitation, DRAc undergoes a rapid ISC to a triplet state with a picosecond time constant, facilitated by a small energy gap between the singlet and triplet states and enhanced by orbital interactions consistent with El-Sayed's rule. These dynamics are further modulated by solvent interactions, particularly hydrogen-bond donation, which stabilizes the singlet excited state ($S_1$) and reduces the energy barrier for ISC.

The ISC process leads to the formation of a radical species, highlighting the photoreactive potential of DRAc. Computational studies confirm that the triplet state is primarily accessed *via* a near-barrierless pathway, influenced by the $\pi\sigma^*$ character of the $S_1$ state and its small energy gap with triplet states at the $S_{1\text{min}}$ geometry. Solvent isotope effects reinforce the role of hydrogen bonding in modulating ISC efficiency, particularly under aqueous conditions.

This study establishes DRAc as a heavy-atom-free model system for ultrafast ISC, demonstrating not only efficient singlet-to-triplet conversion but also the formation of a radical cation species. The ability of DRAc to generate radicals through triplet-state-mediated pathways highlights its potential for photochemical reactivity under mild conditions.

Given its robust ISC dynamics without reliance on heavy atoms, future studies should focus on characterizing the radical's reactivity, stability, and possible role in catalytic or photodynamic applications. In addition, structural modifications—such as incorporating DRAc into the framework of other molecules (as demonstrated by Ramidi *et al.*[52]) or adding substituents to shift its absorption toward longer wavelengths (as demonstrated by Liang *et al.*[53] and Fang *et al.*[54])—could expand its spectral coverage and enhance its suitability for photodynamic therapy (PDT) and related applications.

Expanding this understanding in more complex environments could open new avenues for sustainable photochemical transformations in energy conversion and biomedicine.

## Experimental and computational methods

### Synthesis and sample treatment

The synthesis of the DRAc was previously described by Rocha *et al.*[55]

**Strontium ranelate.** The compound was extracted from Protos®, a drugstore medication containing 2 g of strontium ranelate and 2 g of excipients (aspartame, maltodextrin, and mannitol) per 4 g sachet. To isolate the compound, five sachets were magnetically stirred in 500 mL of distilled water at 50 °C for 4 hours. The solid was decanted, the supernatant removed, and the volume adjusted to 200 mL. This process was repeated twice. In the final cycle, 200 mL of ethanol was added, and the mixture was stirred for 2 hours. The solid was then filtered, vacuum-dried for 12 hours.

**Decarboxyranelic acid (DRAc).** Strontium ranelate (3.5 g) was dissolved in 50 mL of a 6 mol L$^{-1}$ HCl solution in a Petri dish. The dish was kept in the dark for 24 hours. Over the course of a week, the solution was slowly evaporated at ambient temperature and pressure, resulting in the formation of needle-shaped crystals. These crystals were collected by vacuum filtration and washed with 5 mL of diethyl ether. The solid was then dried under vacuum.

### Steady-state spectroscopy

**UV-vis electronic spectroscopy.** The electronic spectra were acquired using a Hewlett-Packard model 8453-A diode array spectrophotometer, using rectangular cuvettes with a 1cm optical path and deuterium and tungsten lamps.

**Raman spectroscopy.** The Raman spectroscopy measurements were performed using a Renishaw Reflex (Invia) spectrometer, with a 365 nm laser, a 2400 lines/mm grating, and a 1024-pixel Renishaw Streamline CCD detector. Before the experiments, the spectrometer was calibrated with a silicon reference standard, achieving a reference peak of (520.5 ± 0.2) cm$^{-1}$. The data acquisition for all measurements was carried out utilizing WiRE 3.4 software.

### Ultrafast transient absorption spectroscopy

A 40-fs pulsed laser with a 3 kHz repetition rate was generated through the Libra Ultrafast Amplifier System designed by Coherent. An optical parametric oscillator (TOPAS-prime, Light Conversion) created the excitation beam. The signals were detected with a UV-NIR detector from Newport MS260i spectrograph with interchangeable gratings. The fundamental laser (probe, 795 nm) passes through the delay stage (1–2 fs step size) and is focused on a $CaF_2$ plate to generate supercontinuum from 300 to 750 nm. The instrument response function obtained for our system is *ca.* 95 fs.

To ensure the constant renovation of the solution, the system employed in this study features a motorized cuvette holder designed to reduce localized photodegradation and improve sample homogeneity during transient absorption spectroscopy. The cuvette is securely held by a mechanical grip and is continuously moved vertically at a frequency of approximately 2 Hz. This continuous motion ensures that different regions of the sample are exposed to the laser beam, preventing prolonged exposure at any single point and minimizing the formation of photoproducts.

### Femtosecond Raman spectroscopy

All the FSRS spectroscopy experiment was conducted on a homebuilt setup constructed around femtosecond Titanium sapphire amplifier Femtopower (Spectra Physics), generating 4.2 mJ pulses of ∼20 fs duration at a repetitive rate of 1 kHz. Another Solstice amplifier (Spectra Physics) sharing both the fs oscillator. Both the Amplifiers were synchronized both by means of electronic and optical delay of the seed prior to amplification. FSRS and TA experiment were integrated in one setup as described below. The experiment is based on controlled time overall of three pulses in the sample, denoted as probe (probing transient absorption and Raman transition), Raman pump (Rp driving sample into vibration coherence with the probe), and actinic pump (Ap – trigger the desired photoreaction).

The probe pulse is generated by splitting the laser output of 0.4 mJ of the laser and used to pump a two stage optical parametric amplifier to generate 1450 nm pulses of ∼40 fs duration. This output was used as a pump for a single filament supercontinuum generated in a 2 mm $CaF_2$ plate, resulting in a white light with the spectrum covering from 370 nm to 1700 nm, near infrared region. The wavelength 1450 nm was chosen to have undesired spike in the probe intensity from the white light driving the pump matching the first peak of water infrared absorption. A 1 cm cuvette with water was used as an efficient notch filter, thus removing the 1450 nm spike resulting in a flat white light covering the whole sensitivity range of the CCD detector. The probe was imaged into the sample by a spherical mirror to a 50 μm diameter spot, from the sample to the detection apparatus.

In detection apparatus, the probe is split into two beams, where one part is sent to a pair of homebuilt grating based high resolution imaging spectrograph for Raman analysis in the Stokes region 750 nm to 950 nm and anti-Stokes region 650 nm to 850 nm. The other part was directed to the prism spectrograph to obtain transient absorption spectra in 370 nm to 1200 nm range. In all the three spectrograph, a 58 × 1024 pixel CCD (Entwicklungsbuero Stresing) was used as a linear image sensor *via* operation in a vertical-binning mode. Cameras were triggered from the lasers at 1 kHz and provided full shot to shot detection with a dynamic range exceeding 30000 : 1. Despite the low intensity of the single filament supercontinuum (∼pJ $nm^{-1}$), it was possible to fully saturate the dynamic range of the sensors. At saturation level, the readout noise of this detector is two orders of magnitude lower than optical short noise at given intensity so, all presented measurement can be considered only optical shot noise limit.

The Raman pump was generated from ∼1.5 mJ of the laser output transmitted *via* a 4f pulse shaper where the spherical disc with 96 shifted aperture was spinning at 10 Hz synchronised with the laser. At a time 15 $cm^{-1}$ interval of wavelength were transmitted by each aperture allowing to produce 96 Raman pulses for each 100 incoming pulses, where each one was shifted by 5 $cm^{-1}$from each other. The shifted signals are then numerically combined to reduce fix pattern noise and facilitate baseline correction. The Raman pulses were generated in the interval from 770 to 795 nm and resulting Raman spectra represents an average of signal from all Raman experiments conducted over this interval. Four pulses out of 100 were fully blocked to produce a pure transient absorption sequence along with the Raman experiment leading to the cyclic scheme where 96% of time the FSRS signal is measured and 4% of time pure TA signal is measured. The Raman pulses were guided *via* an optical delay line and then focused by a lens to ∼100 μm diameter spot overlapped with the probe. Temporal overlap between Raman pump and Probe was adjusted to achieve maximal stimulated Raman gain while maintaining good spectral resolution. Average Raman pulse energy at the sample was ∼4 μJ.

The actinic pulse was generated from 1.5 mJ of the laser output pumping two stage OPA combined with sum frequency generation (TOPAS, light conversion). The 280 nm output was guided *via* a motorized optical delay line and focused into the sample *via* a lens. The actinic pulse energy was adjusted to 2.5 μJ for all experiments.

### Data analysis of time-resolved spectra

Ultrafast transient absorption spectroscopy spectra were analyzed using the Surface Xplorer software. The data window was defined between −0.5 ps and 8000 ps, and the wavelength range was set from 330 nm to 700 nm. Following the correction for probe velocity dispersion (chirp correction), the kinetic traces were extracted and fitted using a mathematical model (see SI).

### Molecular modelling

The ground state and excited state geometry optimizations, as well as their associated vibrational frequencies and orbitals energies were obtained from DFT and TD-DFT calculations performed with the GAUSSIAN 16 package.[56] The calculation employed the hybrid exchange functional of Becke with the correlation functional of Lee, Yang and Parr (B3LYP[57–59]), and the 6-311++(d,p) split-valence triple-ζ basis set in the polarizable continuum model (PCM) using the integral equation formalism variant (IEFPCM) using water and methanol as solvent. The discussion and references supporting the functional choice are provided in the SI. Default SCF convergence criteria were used (tight convergence), and geometry optimizations used the default convergence thresholds in Gaussian 16 (maximum force $4.5 \times 10^{-4}$ a.u., RMS force $3.0 \times 10^{-4}$ a.u., maximum displacement $1.8 \times 10^{-3}$ a.u., and RMS displacement $1.2 \times 10^{-3}$ a.u.). Numerical quadrature grids used the default ''FineGrid'' setting in Gaussian 16.

To construct the schematic representation of potential energy (PE) curves, it was essential to ascertain the energy minimum of the respective state, followed by the determination of the energies of the other relevant states.

The optimized geometries for the singlet ground state ($S_0$) and the first triplet state ($T_1$) were obtained using DFT and unrestricted DFT (UDFT), respectively, while TD-DFT was employed for the first excited state ($S_1$), utilizing the B3LYP/6-311++(d,p) basis set. Subsequently, TD-DFT calculations were performed to evaluate the vertical excitation energies of the excited states within this optimized geometry. To facilitate the identification of each state across varying geometries, a natural transition orbital (NTO) population analysis was conducted, providing insights into the electronic transitions involved.

## Author contributions

Luca M. Sihn: investigation, data curation, visualization, writing – original draft. Robert B. Vadellb: conceptualization, investigation. Rafael B. Araujoc: methodology, investigation. Atripan Mukherjeed: investigation, data curation. Miroslav Kloze: data curation, resources. Jacinto Sá: supervision, resources, writing – review & editing. Henrique Eisi Toma: supervision, funding acquisition.

## Conflicts of interest

There are no conflicts to declare.

## Data availability

All computed energy data, optimized geometries, and additional supporting results are available in the SI. The SI includes comprehensive tables (Tables S1–S5) detailing the state energies of DRAc's main excited states at various geometries and solvent models, figures (Fig. S1–S4 and FSRS traces) that illustrate the temporal evolution of the $S_1$ and $T_1$ states, the fitted kinetic traces at distinct wavelengths and the corresponding fitted $T_1$ population curves in $D_2O$, $CD_3OD$, $H_2O$, and $CH_3OH$ (all at 3 mol $L^{-1}$ HCl). Alongside this, discussions are also presented on the mathematical model used to fit the kinetics, the methodology employed to extract the $S_1$ and $T_1$ population curves, and considerations regarding the use of the B3LYP functional. Complete atomic coordinates for representative geometries (*e.g.*, $H_2O$ implicit/explicit models, $CH_3OH$) are provided in.xyz format within the DRAc_Geometries.zip archive in the SI. See DOI: **https://doi.org/10.1039/d5cp01512j**

## Acknowledgements

The authors acknowledge financial support from the São Paulo Research Foundation (FAPESP) under grant numbers 18/21489-1 and 18/25974-1. We also thank the Extreme Light Infrastructure (ELI) in Prague for providing access to FSRS analyses. This research was additionally supported by the Czech Science Foundation (project no. 21-09692M). Special thanks to César Rui Bernardo for technical support. Computational resources were provided by the National Academic Infrastructure for Supercomputing in Sweden (NAISS) under project NAISS 2024/5-372.

## Notes and references

1 E. del Pino Rosendo, O. Yildiz, W. Pisula, T. Marszalek, P. W. M. Blom and C. Ramanan, *Phys. Chem. Chem. Phys.*, 2023, **25**, 6847–6856.

2 L. Yang, X. Wang, G. Zhang, X. Chen, G. Zhang and J. Jiang, *Nanoscale*, 2016, **8**, 17422–17426.

3 Z. Xu, Y. Jiang, Y. Shen, L. Tang, Z. Hu, G. Lin, W. C. Law, M. Ma, B. Dong, K. T. Yong, G. Xu, Y. Tao, R. Chen and C. Yang, *Mater. Horiz.*, 2022, **9**, 1283–1292.

4 E. Bassan, A. Gualandi, P. G. Cozzi and P. Ceroni, *Chem. Sci.*, 2021, **12**(19), 6607–6628.

5 D. A. McQuarrie and J. D. Simon, *Physical chemistry: a molecular approach*, University Science Books, 1997.

6 T. Moitra, P. Karak, S. Chakraborty, K. Ruud and S. Chakrabarti, *Phys. Chem. Chem. Phys.*, 2021, **23**(1), 59–81.

7 S. P. Pitre, C. D. McTiernan, H. Ismaili and J. C. Scaiano, *J. Am. Chem. Soc.*, 2013, **135**, 13286–13289.

8 E. Speckmeier, T. G. Fischer and K. Zeitler, *J. Am. Chem. Soc.*, 2018, **140**, 15353–15365.

9 N. J. Treat, H. Sprafke, J. W. Kramer, P. G. Clark, B. E. Barton, J. Read De Alaniz, B. P. Fors and C. J. Hawker, *J. Am. Chem. Soc.*, 2014, **136**, 16096–16101.

10 B. G. McCarthy, R. M. Pearson, C. H. Lim, S. M. Sartor, N. H. Damrauer and G. M. Miyake, *J. Am. Chem. Soc.*, 2018, **140**, 5088–5101.

11 S. Xu, Y. Yuan, X. Cai, C. J. Zhang, F. Hu, J. Liang, G. Zhang, D. Zhang and B. Liu, *Chem. Sci.*, 2015, **6**, 5824–5830.

12 D. A. Nicewicz and T. M. Nguyen, *ACS Catal.*, 2014, **4**(1), 355–360.

13 C. Li, Y. Xu, W. Tu, G. Chen and R. Xu, *Green Chem.*, 2017, **19**(4), 882–899.

14 M. A. Filatov, *Org. Biomol. Chem.*, 2019, **18**(1), 10–27.

15 V. N. Nguyen, Y. Yan, J. Zhao and J. Yoon, *Acc. Chem. Res.*, 2021, **54**, 207–220.

16 S. Bhowmik, A. Dutta and P. Sen, *J. Phys. Chem. A*, 2024, **128**, 6864–6878.

17 S. Siegert, F. Vogeler, C. M. Marian and R. Weinkauf, *Phys. Chem. Chem. Phys.*, 2011, **13**, 10350–10363.

18 R. Englman and J. Jortner, *Mol. Phys.*, 1970, **18**, 285–287.

19 Y. R. Poh, S. Pannir-Sivajothi and J. Yuen-Zhou, *J. Phys. Chem. C*, 2023, **127**, 5491–5501.

20 C. Prentice, A. E. Martin, J. Morrison, A. D. Smith and E. Zysman-Colman, *Org. Biomol. Chem.*, 2023, **21**, 3307–3310.

21 R. K. Venkatraman and A. J. Orr-Ewing, *Acc. Chem. Res.*, 2021, **54**, 4383–4394.

22 P. Pokhilko and A. I. Krylov, *J. Phys. Chem. Lett.*, 2019, **10**, 4857–4862.

23 J. C. Rocha, L. M. Sihn, M. K. Uchiyama, M. A. Ribeiro, M. P. Franco, A. A. C. Braga, A. T. Silveira and H. E. Toma, *ChemistrySelect*, 2019, **4**(47), 13926–13931.

24 N. Chattopadhyay, S. J. Quinn, O. Kifor, C. Ye and E. M. Brown, *Biochem. Pharmacol.*, 2007, **74**, 438–447.

25 N. Chattopadhyay, S. J. Quinn, O. Kifor, C. Ye and E. M. Brown, *Biochem. Pharmacol.*, 2007, **74**, 438–447.

26 W. Han, S. Fan, X. Bai and C. Ding, *Expert Opin. Invest. Drugs*, 2017, **26**, 375–380.

27 P. J. Marie, *Bone*, 2007, **40**(5), 5–8.

28 J. C. da Rocha, J. V. Mattioni, L. M. Sihn, J. S. Shinohara, F. M. Melo, M. P. Franco, A. A. C. Braga and H. E. Toma, *J. Raman Spectrosc.*, 2020, **51**, 1083–1091.

29 G. M. Blake and I. Fogelman, *Clin. Interventions Aging*, 2006, **1**, 367–375.

30 W. Hongtao, C. Jin, S. Min and J. Min, *Heteroat. Chem.*, 2007, **18**, 236–238.

31 L. M. Sihn, E. L. Bastos, M. Nakamura, M. K. Uchiyama and H. E. Toma, *Colorants*, 2023, **2**, 578–590.

32 A. Prlj, B. F. E. Curchod and C. Corminboeuf, *Phys. Chem. Chem. Phys.*, 2015, **17**, 14719–14730.

33 M. A. Parkes and G. A. Worth, *J. Chem. Phys.*, 2024, **161**(11), 114305.

34 A. M. Kelley, *J. Phys. Chem. A*, 2008, **112**, 11975–11991.

35 S. Gómez, N. Rojas-Valencia, T. Giovannini, A. Restrepo and C. Cappelli, *Molecules*, 2022, **27**(2), 442.

36 E. V. Efremov, F. Ariese and C. Gooijer, *Anal. Chim. Acta*, 2008, **606**(2), 119–134.

37 S. M. Sun, S. Zhang, K. Liu, Y. P. Wang and B. Zhang, *Photochem. Photobiol. Sci.*, 2015, **14**, 853–858.

38 J. Pina, M. J. R. P. Queiroz and J. Seixas De Melo, *Photochem. Photobiol. Sci.*, 2016, **15**, 1029–1038.

39 R. Weinkauf, L. Lehr, E. W. Schlag, S. Salzmann and C. M. Marian, *Phys. Chem. Chem. Phys.*, 2008, **10**, 393–404.

40 S. M. Sun, S. Zhang, K. Liu, Y. P. Wang and B. Zhang, *Photochem. Photobiol. Sci.*, 2015, **14**, 853–858.

41 D. Grebner, M. Helbig and S. Rentsch, *Size-Dependent Properties of Oligothiophenes by Picosecond Time-Resolved Spectroscopy*, 1995, vol. 99.

42 I. L. Zheldakov, J. M. Wasylenko and C. G. Elles, *Phys. Chem. Chem. Phys.*, 2012, **14**, 6211–6218.

43 M. J. Kamlet, J.-L. M. Abboud, M. H. Abraham and R. W. Taft, *Solvent Effects in Organic Chemistry*, UTC, 1983, vol. 48.

44 M. A. El-Sayed, *J. Chem. Phys.*, 1962, **36**(2), 573–574.

45 C. M. Marian, Annual Review of Physical Chemistry Downloaded from **https://www.annualreviews.org**. Guest, 2024, 36, 45.

46 S. Scheiner and M. C. Uma, Relative Stability of Hydrogen and Deuterium Bonds, 1996.

47 Y. C. Wei, S. F. Wang, Y. Hu, L. S. Liao, D. G. Chen, K. H. Chang, C. W. Wang, S. H. Liu, W. H. Chan, J. L. Liao, W. Y. Hung, T. H. Wang, P. T. Chen, H. F. Hsu, Y. Chi and P. T. Chou, *Nat. Photonics*, 2020, **14**, 570–577.

48 A. S. Mereshchenko, O. S. Myasnikova, M. S. Panov, V. A. Kochemirovsky, M. Y. Skripkin, D. S. Budkina and A. N. Tarnovsky, *J. Phys. Chem. B*, 2017, **121**, 4562–4568.

49 W. R. Browne and J. G. Vos, The effect of deuteriation on the emission lifetime of inorganic compounds, 2001.

50 T. A. P. Hai and R. Sugimoto, *Catal. Lett.*, 2017, **147**, 1955–1965.

51 S. V. Kamat, V. Puri and R. K. Puri, *Phys. Scr.*, 2011, **84**(4), 045801.

52 P. Ramidi, O. Abdulrazzaq, C. M. Felton, Y. Gartia, V. Saini, A. S. Biris and A. Ghosh, *Energy Technol.*, 2014, **2**, 604–611.

53 X. Liang, S. Shimizu and N. Kobayashi, *Chem. Commun.*, 2014, **50**, 13781–13784.

54 Z. Fang, X. Zhang, F. Wu, B. Huang, Z. Cao and B. Yi, *J. Mol. Liq.*, 2024, **412**, 125630.

55 J. C. Rocha, L. M. Sihn, M. K. Uchiyama, M. A. Ribeiro, M. P. Franco, A. A. C. Braga, A. T. Silveira and H. E. Toma, *ChemistrySelect*, 2019, **4**, 13926–13931.

56 M. J. Frisch, G. W. Trucks, H. B. Schlegel, G. E. Scuseria, M. A. Robb, J. R. Cheeseman, G. Scalmani, V. Barone, G. A. Petersson, H. Nakatsuji, X. Li, M. Caricato, A. V. Marenich, J. Bloino, B. G. Janesko, R. Gomperts, B. Mennucci, H. P. Hratchian, J. V. Ortiz, A. F. Izmaylov, J. L. Sonnenberg, D. Williams-Young, F. Ding, F. Lipparini, F. Egidi, J. Goings, B. Peng, A. Petrone, T. Henderson, D. Ranasinghe, V. G. Zakrzewski, J. Gao, N. Rega, G. Zheng, W. Liang, M. Hada, M. Ehara, K. Toyota, R. Fukuda, J. Hasegawa, M. Ishida, T. Nakajima, Y. Honda, O. Kitao, H. Nakai, T. Vreven, K. Throssell, J. A. Montgomery Jr., J. E. Peralta, F. Ogliaro, M. J. Bearpark, J. J. Heyd, E. N. Brothers, K. N. Kudin, V. N. Staroverov, T. A. Keith, R. Kobayashi, J. Normand, K. Raghavachari, A. P. Rendell, J. C. Burant, S. S. Iyengar, J. Tomasi, M. Cossi, J. M. Millam, M. Klene, C. Adamo, R. Cammi, J. W. Ochterski, R. L. Martin, K. Morokuma, O. Farkas, J. B. Foresman and D. J. Fox, 2016.

57 A. D. Becke, *J. Chem. Phys.*, 1993, **98**, 5648–5652.

58 P. J. Stephens, F. J. Devlin, C. F. Chabalowski and M. J. Frisch, *J. Phys. Chem.*, 1994, **98**, 11623–11627.

59 C. Lee, W. Yang and R. G. Parr, *Phys. Rev. B: Condens. Matter Mater. Phys.*, 1988, **37**, 785–789.